Article

Enhanced Photocatalytic CO$_2$ Reduction to CH$_4$ Using Novel Ternary Photocatalyst RGO/Au-TNTAs

Md. Arif Hossen [1,2], Fatema Khatun [1], Riyadh Ramadhan Ikreedeegh [3,4], Aamina Din Muhammad [1], Azrina Abd Aziz [1,*], Kah Hon Leong [5,*], Lan Ching Sim [6], Wu Lihua [7] and Minhaj Uddin Monir [8]

1   Faculty of Civil Engineering Technology, Universiti Malaysia Pahang, Gambang 26300, Pahang, Malaysia; arifhossen0101@cuet.ac.bd (M.A.H.); lubna.pme71@gmail.com (F.K.); aaminapathan.energy@gmail.com (A.D.M.)
2   Center for Environmental Science & Engineering Research, Chittagong University of Engineering and Technology, Chattogram 4349, Bangladesh
3   Department of Analysis and Quality Control, Sarir Oil Refinery, Arabian Gulf Oil Company, Benghazi P.O. Box 263, Libya; riyadhkridiegh@gmail.com
4   Chemical Reaction Engineering Group (CREG), School of Chemical and Energy Engineering, Universiti Teknologi Malaysia (UTM), Johor Bahru 81310, Johor, Malaysia
5   Department of Environmental Engineering, Faculty of Engineering and Green Technology, Universiti Tunku Abdul Rahman, Kampar 31900, Perak, Malaysia
6   Department of Chemical Engineering, Lee Kong Chian Faculty of Engineering and Science, Universiti Tunku Abdul Rahman, Kajang 43200, Selangor, Malaysia; simcl@utar.edu.my
7   Kuantan Sunny Scientific Collaboration Sdn. Bhd. Suites 7.23, 7th Floor, Imbi Plaza, Jalan Imbi, Kuala Lumpur 55100, Kuala Lumpur, Malaysia; wulihua217@gmail.com
8   Department of Petroleum and Mining Engineering, Jashore University of Science and Technology, Jashore 7408, Bangladesh; monir_pme@just.edu.bd
*   Correspondence: azrinaaziz@ump.edu.my (A.A.A.); khleong@utar.edu.my (K.H.L.)

Abstract: Photocatalytic CO$_2$ reduction into hydrocarbon fuels is one of the most efficient processes since it serves as a renewable energy source while also lowering atmospheric CO$_2$ levels. The development of appropriate materials and technology to attain greater yield in CO$_2$ photoreduction is one of the key issues facing the 21st century. This study successfully fabricated novel ternary reduced graphene oxide (RGO)/Au-TiO$_2$ nanotube arrays (TNTAs) photocatalysts to promote CO$_2$ photoreduction to CH$_4$. Visible light-responsive RGO/Au-TNTAs composite was synthesized by facile electrochemical deposition of Au nanoparticles (NPs) and immersion of RGO nanosheets onto TNTAs. The synthesized composite has been thoroughly investigated by FESEM, HR-TEM, XRD, XPS, FT-IR, UV-Vis DRS, and PL analyzer to explain structural and functional performance. Under the source of visible light, the maximum yield of CH$_4$ was attained at 35.13 ppm/cm^2 for the RGO/Au-TNTAs composite photocatalyst after 4 h, which was considerably higher by a wide margin than that of pure TNTAs, Au-TNTAs and RGO-TNTAs. The CO$_2$ photoreduction of the RGO/Au-TNTAs composite has been improved due to the combined effects of Au NPs and RGO. Due to its surface plasmonic resonance (SPR) mechanism, Au NPs play a crucial role in the absorption of visible light. Additionally, the middle RGO layers serve as effective electron transporters, facilitating better separation of electron-hole pairs. The newly constructed composite would be a promising photocatalyst for future photocatalytic applications in other fields.

Keywords: photocatalytic CO$_2$ reduction; CH$_4$ production; TNTAs; Au NPs; RGO; LSPR effect

1. Introduction

The high consumption of fossil fuels will lead to a serious global energy crisis in the future [1–5]. It is estimated that our demand for these non-renewable sources will rise to 56% by 2040 [6–8]. Moreover, burning of these fuels generates massive amounts of greenhouse gases (mainly carbon dioxide) in the atmosphere leading to many environmental problems

including climate change, global warming, acid rains, sea level rise, and health-related problems [9–12]. Therefore, finding an efficient and sustainable energy source is highly needed in the future. Photocatalytic carbon dioxide (CO_2) reduction into valuable fuels through solar light-assisted energy is regarded as one of the most promising technologies for the mitigation of CO_2 gas and partially fulfilling energy demands [13–16]. Among all semiconductors, titanium dioxide (TiO_2) has been employed as a typical photocatalyst, owing to its low cost, high corrosion resistance, strong redox ability, and good chemical stability [17–20]. However, TiO_2 exhibits low photocatalytic production yields because of its higher rate of recombination of photoexcited charges and low visible light harvesting.

Recently, the TiO_2 in the form of nanotube arrays (TNTAs) has attracted much attention due to the advantage of orthogonalization of light absorption by offering more scattering and trapping of light [21]. Moreover, the TiO_2 nanotube system facilitates the flow of electrons among the nanotube walls providing more shortcuts compared to lengthened electron pathways in nanoparticle systems [22–24]. However, the TNTAs photocatalyst still performs poorly under visible light due to its wide band gap (3.0–3.2 eV) which limits its application only to the UV range. Tremendous efforts have been devoted to addressing these TNTAs drawbacks through various strategies such as band gap engineering [25,26], coupling with metals and metal oxides [27,28], and doping with inorganic and organic materials [29,30]. However, the incorporation of TNTAs with noble metals such as silver (Ag), platinum (Pt), and gold (Au) was found to be the most effective strategy to enhance the photocatalytic performance by suppressing the recombination of photogenerated charges [31,32]. This photocatalytic enhancement is attributed to the unique characteristic of localized surface plasmon resonance (LSPR). Briefly, when the oscillation frequency of noble meals free electrons is matched with the wavelength of the incident light, the LSPR effect is induced, generating a high population of energetic electrons known as hot electrons. These electrons are then transported to the neighboring semiconductor material (TNTAs) and participated in the redox photocatalytic reactions [33,34]. Khatun et al. [35] have successfully incorporated TNTAs with Au nanoparticles (NPs) through a facile electrochemical deposition method for improving the photocatalytic CO_2 conversion into CH_4 under visible light. A binary component of Pt/Au NPs was also deposited on TNTAs by Pan et al. [36] and displayed outstanding performance for photocatalytic CO_2 reduction. In a very recent study, Montakhab and coworkers [37] reported the decoration of TNTAs with Ag NPs for enhanced TNTAs photodegradation efficiency under UV and visible light.

The incorporation of carbon-based materials along with noble metals to TNTAs acts as an electron mediator for promoting the transfer and separation of charge carriers [38–40]. In the TiO_2-based composite photocatalysts, both graphene and reduced graphene oxide (GO and RGO) are considered emerging photosensitizers that effectively enhance visible light absorption [41,42]. Devi et al. [43] reported the use of pt-coated, GO-wrapped TNTAs for enhanced photocatalytic CO_2 conversion to CH_4. The photocatalytic CO_2 reduction performance over Au-TNTAs, and RGO-TNTAs binary nanocomposites has been extensively studied. However, the performance of ternary RGO/Au-TNTAs photocatalysts under visible light is still unexplored and has not been reported yet.

In this study, a well-designed RGO/Au-TNTAs ternary nanocomposite was successfully fabricated using a facile method of electrochemical anodization and immersion deposition. The novel ternary photocatalyst was tested for photocatalytic CO_2 reduction under visible light and displayed both enhanced characterization and better experimental results compared to pure TNTAs. Finally, a simple mechanism has been proposed and well explained to provide a clear understanding of the photocatalytic process over the RGO/Au-TNTAs nanocomposite. This research provides a step forward in synthesizing highly efficient noble metal-modified TNTAs photocatalyst systems for the conversion of CO_2 into valuable fuels through solar light-assisted energy.

2. Experimental Overview

2.1. Reagents and Materials

Analytical grade substances were employed in this study and utilized as received from Sigma-Aldrich Chemicals Company without any further purification. To prepare TNATs, titanium (Ti) foils with 0.127 mm thickness (99.97%) were used. Ammonium fluoride (NH_4F, 98.0%), ethylene glycol (EG, 99.5%), and gold (III) chloride hydrate ($HAuCl_4$, 99.99%) were used to prepare the electrolyte solutions. Natural graphite powder (99.99%), sulphuric acid (H_2SO_4, 97%), hydrochloric acid (HCl, 37%), phosphoric acid (H_3PO_4, 85%), hydrogen peroxide (H_2O_2, 30%) and potassium permanganate ($KMnO_4$, 99.39%) were used to synthesise graphene oxide (GO). Ethyl alcohol (95%), acetone (99.5%), and purified water obtained with the Nanopure® water system of Thermo Fisher Scientific were utilized for all cleaning purposes prior to any experiment using ultrasonic cleaner (JAC-1020 P). A DC power supply (GPS-3030DD, GW Instek) was employed for the anodization process. Finally, a muffle furnace (WiseTherm®, version 1.3.1) was employed for annealing purposes.

2.2. Preparation of TNT Arrays

The TNTAs layer was formed on the Ti foil using an electrochemical anodization method as reported in our previous study with slight modification [44]. In brief, a Ti foil (14 mm × 13 mm) was used as a working electrode in 65 mL EG containing electrolyte comprising 720 mg NH_4F and 1.3 mL pure water. To get TNTAs on the Ti-substrate, a steady voltage of 25 V was applied for approximately 3 h. A counter electrode of graphite rod was employed. The as-prepared Ti nanotubes were amorphous. Hence, to get crystalline TNTAs, the as-anodized sample was annealed in a programmable furnace for 2 h at 450 °C.

2.3. Preparation of Au-Deposited TNT Arrays

A facile electrochemical deposition method was utilized for the deposition of Au nanoparticles into TNTAs. A previously reported experimental procedure [35] was followed with slight modification. In precise, the as-prepared TNTAs sample was utilized as a cathode while a Ti foil was employed as an anode. The anodization process was conducted at room temperature using a 125 mL EG electrolyte containing 0.125 g of $HAuCl_4$ and under a voltage of 4 V for 3 min. Finally, the anodized Ti foil was rinsed, dried, and annealed for 2 h at 550 °C so that hierarchical, well-ordered, Au-deposited TiO_2 nanotube arrays are obtained.

2.4. Preparation of GO and RGO

Natural graphite powder was used to prepare graphene oxide (GO) nanosheets through Tour's method [45]. Briefly, a certain amount (3 g) of graphite powder was oxidized by an acidic solution of concentrated H_2SO_4 and H_3PO_4 acids (360:40 mL) with a continuous stirring at 300 rpm in an oil bath. Then, $KMnO_4$ (18 g) was gradually added to the mixture in order to keep the reaction temperature at 50 °C. Consequently, the continuous oxidation was performed for 24 h, after that the obtained suspension was cooled down to normal temperature, and ice (400 mL) has been poured into the suspension. Additionally, A total of 3 mL of H_2O_2 was slowly added into the suspension dropwise. Then, the suspension was centrifuged, washed several times for the removal of any leftover impurities, and dried overnight at 60 °C to obtain pure blackish nanosheets of GO. The reduced graphene oxide (RGO) was prepared through a thermal treatment of GO powder in which 3 mg of graphene oxide was heated in a preheated furnace at 300 °C for 3 min to deliver a single layer structure of blackish exfoliated RGO nanosheets.

2.5. Preparation of Au and RGO-Modified TNTAs (RGO/Au-TNTAs)

The RGO-TNTAs and RGO/Au-TNTAs composites were fabricated through a facile immersion method. For the RGO-TNTAs composite, a pure TNTAs sample was immersed for 3 h in RGO suspension prepared with 20 min sonication of 4 mL water and 2 mg of RGO powder. The sample was then dried in an oven for 5 h at 60 °C and denoted as

RGO-TNTAs. However, the ternary RGO/Au-TNTAs photocatalyst was synthesized with a 4 h continuous immersion of Au-TNTAs sample in RGO suspension containing 1 mg of RGO and 2 mL of pure water. Finally, the sample was dried in an oven for 5 h at 60 °C and denoted as RGO/Au-TNTAs. Figure 1 shows the whole synthesis procedure of the ternary RGO/Au-TNTAs photocatalyst.
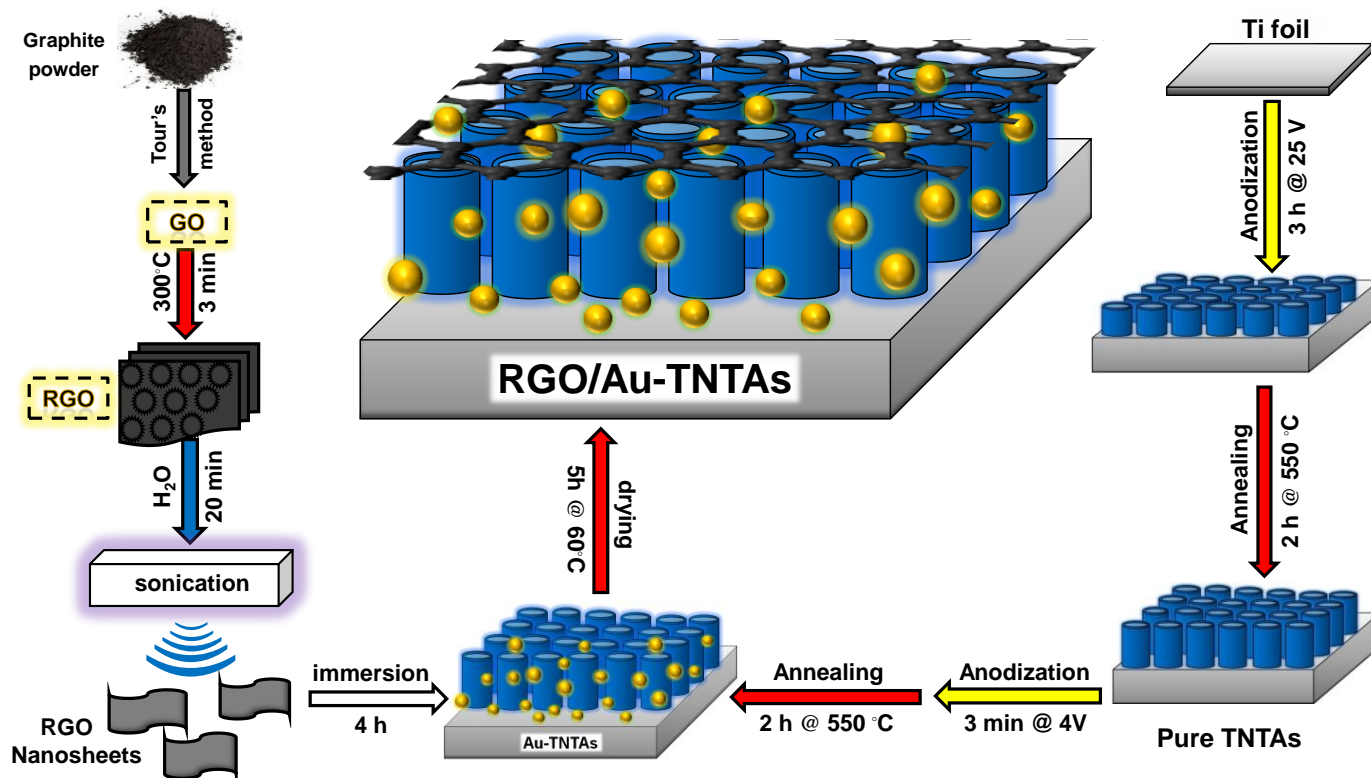

Figure 1. Schematic illustration for the synthesis procedure of RGO/Au-TNTAs photocatalyst.

2.6. Characterization

The physical structures and surface morphologies of the synthesized samples were characterized using a field emission scanning electron microscope (FESEM) equipped with an energy dispersive X-ray (EDX) spectroscopy detector, operating at a voltage of 20 kV (Brand: JEOL, Model: JSM-7800F). The lattice structure and the nanoparticles size were identified with the High-resolution Transmission Electron Microscope (HRTEM) operating at 200 kV voltage (Brand: Fei, Model: Tecnai-G2-20-Twin). An X-ray diffractometer (XRD) of Bruker brand model D8 advance was employed to investigate the crystalline structure of the newly developed composites with a Cu Kα radiation source, 40 mA current, and 40 kV voltage. The chemical elemental species mapping and identification were acquired from X-ray Photoelectron Spectroscopy Analysis (XPS) (Brand: PHI, Model: 5000 VersaProbeII). The functional groups in the prepared samples were investigated through the Fourier-transform infrared spectroscope (FTIR) of the Perkin Elmer brand model Spectrum 100. The visible light harvesting characteristics were studied with UV–vis diffuse reflectance (UV-Vis DRS) spectrophotometer having wavelength ranging from 200 to 800 nm (Brand: SHIMADZU, Model: UV, 2600-230V). The photoluminescence (PL) spectra of the prepared samples were performed through PL spectra with emitted laser beams of 325 nm (Brand: EDINBURGH INSTRUMENTS, Model: NIR 300/2).

2.7. Quantification of Photocatalytic CO$_2$ Reduction

The photocatalytic CO$_2$ reduction process was carried out using a gas-phase photo-reactor with a photocatalytic set-up as illustrated in Figure 2. A 300 W xenon lamp fitted with a reflector was used as a visible light source with a light intensity of 100 Wm^{-2}. The

prepared photocatalysts were placed inside the photoreactor chamber. The whole system was purged with N_2 gas before any reactions to remove any trace gases and impurities. Then a decidedly purified CO_2 gas (99.99%) has been passed through the water bubbler at room temperature and to the reaction chamber maintaining a flow rate of 50 mL min^{-1} until a pressure of 100 kPa was attained. The lamp was switched on to start the photoreduction process at room temperature and after 4 h of light irradiation, a gas product sample was collected for every 1h intervals and analyzed by using a gas chromatograph (AGILENT, Model: 7890A) equipped with a 25 m capillary column (AGILENT, PoraPLOT) and a flame ionization detector (AGILENT, Model: 7890A) for the detection of CH_4 gas. However, the production rate of CH_4 gas was calculated using Equation (1), as described in previous studies [46,47].

$$\text{Rate of } CH_4 \text{ generation} = \frac{Amount\ of\ CH_4\ produced\ in\ \text{ppm}}{Exposed\ area\ of\ photocatalyst\ (\text{cm}^2) \times time\ (\text{h})} \tag{1}$$
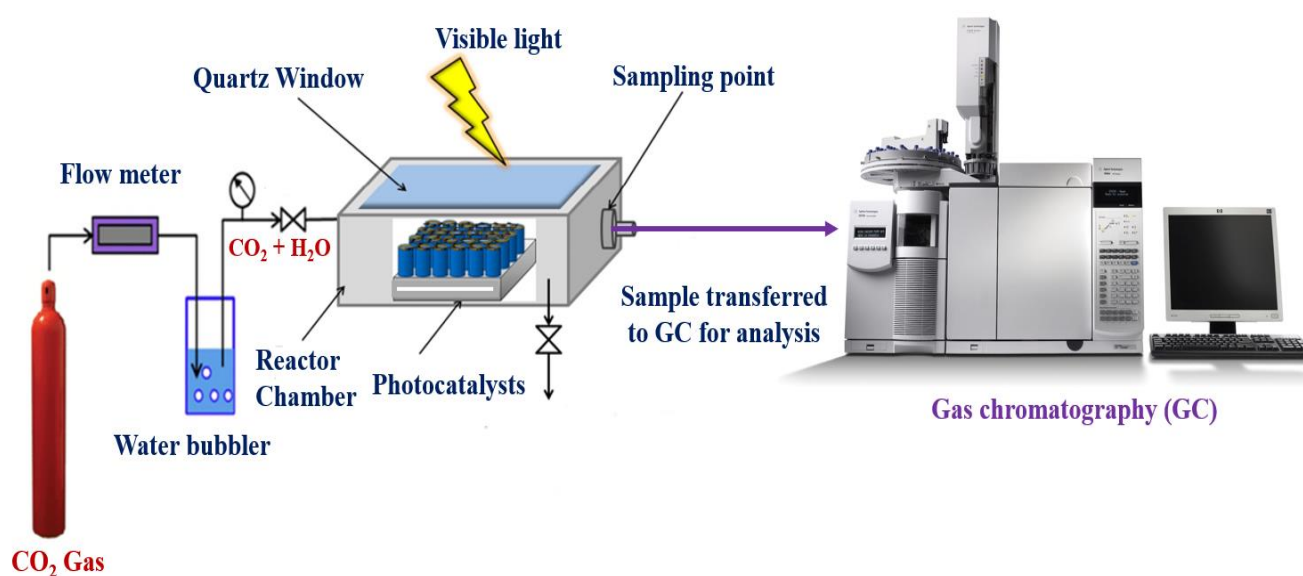

Figure 2. Schematic illustration of gas-solid phase photoreactor set-up.

3. Results and Discussion

3.1. Morphological Characterization

The surface morphologies of the prepared photocatalysts were investigated in detail through the FESEM analysis as presented in Figure 3. The TNTAs photocatalyst acted as the base material for the deposition of other nanocomposite photocatalysts. The FESEM images of pure TNTAs are shown in Figure 3a–c. As shown in Figure 3a, a top-view image of self-organized and well-aligned TiO_2 nanotubes has been clearly attained through FESEM analysis. Figure 3b shows an image of open-pore TiO_2 nanotubes that are well-attached to each other with an average inner diameter of 60 ± 4 nm. A cross-sectional view image is depicted in Figure 3c, revealing an efficient growth of one-dimensional, vertically oriented TiO_2 nanotubes over the Ti metal substrate with an excellent tube-length reaching up to 900 nm. The higher length of TiO_2 nanotubes provides more chances for contact between the nanotubes with the CO_2 and H_2O molecules [23,48]. These morphological results of TNTAs are consistent with the literature reported by Ikreedeegh & Tahir [23], Devi et al. [43], Sim et al. [49], Low et al. [50], and Lee and Kim [51], revealing the proper anodization with sufficient annealing for achieving hierarchical, vertically orientated, free of surface-damage and open-pores TNTAs.
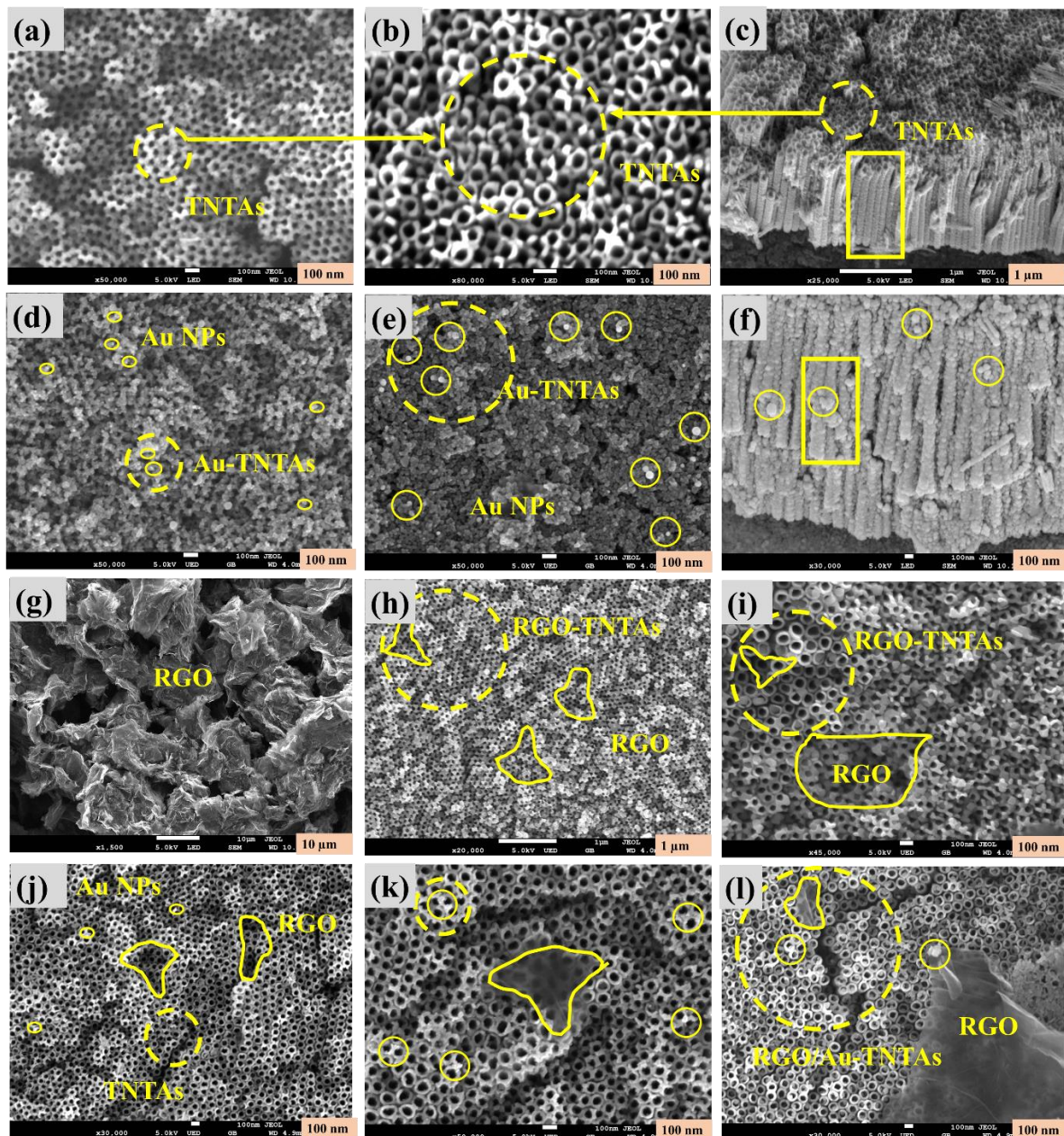
Figure 3. FESEM images of (**a**,**b**) Pure TNTAs at different magnifications (**c**) Cross-sectional view of pure TNTAs, (**d**,**e**) Surface view of Au-TNTAs composite (**f**) Cross-sectional view of Au-TNTAs composite, (**g**) Pure RGO surface, (**h**,**i**) RGO-TNTAs at different magnification and (**j**–**l**) Surface view of RGO/Au-TNTAs composite at different magnification.

The Au nanoparticles have been successfully incorporated into the nanotubes through the electrochemical deposition method. Figure 3d–f shows clearly the decoration of the nanotubes mouth and walls with the Au nanoparticles (NPs). The crystalline size of Au NPs was calculated to be 8 nm through the XRD analysis, while an average diameter of 60 nm was exhibited by the nanotubes. Due to the dispersion of Au nanoparticles over TNT layers during electrochemical deposition the mouth of TNTAs remained clogged in some places [52,53]. However, RGO sheets have been assembled onto Au-TNTAs which balanced the Au NPs deposition on TNTAs. Figure 3g–i shows the pure RGO surface and RGO-TNTAs composite at different magnifications. Due to the high recombination rate of photogenerated charges associated with the TiO_2, reduced graphene oxide (RGO) has been incorporated into both TNTAs and Au-TNTAs. Eventually, the presence of well-

dispersed RGO nanosheets would be beneficial for the efficient separation and transfer of photogenerated electron-hole pairs [54,55]. Figure 3j–l shows clearly the presence of a homogeneously deposited transparent RGO nanosheet with Au NPs on the top of the nanotubes. The clear observation of the RGO/Au-TNTAs in FESEM image demonstrated that the TNTAs remained unchanged after the inclusion of both Au NPs and RGO nanosheets. The one-dimensional (1D) TiO_2 nanotubes with zero-dimensional (0D) deposited Au NPs and the assembled two-dimensional (2D) transparent RGO nanosheets would provide a larger surface area for the adsorption of both CO_2 and water molecules. Moreover, the uniform distribution of Au NPs can provide more LSPR zones for improving the photocatalytic reaction.

The elemental analysis of TNTAs, Au-TNTAs, RGO-TNTAs and RGO/Au-TNTAs is obtained through EDX analysis and presented in Figure S1a–1d. To ensure that Au and RGO were evenly distributed and dispersed across the surface of the TNTAs plate, the EDX analysis was carried out over several spots of the surface. As shown in Figure S1a, the EDX results of TNTAs exhibited the presence of major elements like Ti and O. Figure S1b confirms the presence of Ti, O and Au elements in Au-TNTAs photocatalysts. The EDX analysis of RGO-TNTAs is displayed in Figure S1c and it revealed the good quality of RGO through the elemental existence of Ti, O, and C without any impurities being detected. The EDX mapping confirmed the presence of all specific elements like Au, C, Ti, and O in the ternary RGO/Au-TNTAs composite with different atomic ratios of 7.3%, 12.4%, 61.1%, and 19.2%, respectively.

To provide additional evidence of the existence of Au NPs and RGO in the inner space of the TNTAs, all of the prepared samples were examined by the HR-TEM. The HR-TEM images of TNTAs, Au-TNTAs and RGO/Au-TNTAs are presented in Figure 4a–i. Figure 4c reveals the lattice fringe of pure TNTAs by exhibiting a *d*-spacing of 0.35 nm, corresponding to the plane (101) of TiO_2 anatase phase (DB card number 7206075). Similar *d*-spacing values of 0.35 nm for TNTAs wall surface were also reported by Sim et al. [56], Goddeti et al. [57], and Zubair et al. [47]. Au NPs were homogeneously distributed in the TNTAs and deposited inside the nanotubes as shown in Figure 4f. However, the interlayer spacing of 0.24 nm can be indexed to the Au (111) lattice plane (DB card number 9008463). In this work, RGO incorporation with the Au-TNTAs has been reported for the first time to improve the photocatalytic CO_2 reduction performance. The transparent RGO nanosheet was obvious in Figure 4g,h. After the incorporation of Au NPs and RGO into TNTAs, the lattice fringes of TNTAs and Au NPs in the ternary RGO/Au-TNTAs composite exhibited the same results obtained with the pure TNTAs and Au-TNTAs samples. These observations were also conceding with the next XRD results.

XRD analysis is used to justify the average spacing of two crystal planes of the synthesized samples as well as their crystal structure. The diffraction patterns of the synthesized TNTAs (before and after annealing), bare RGO, RGO-TNTAs, Au-TNTAs, and RGO/Au-TNTAs nanocomposites are depicted in Figure 5. Before annealing TNTs were in the amorphous phase, no peak was detected for anatase or rutile. The TNTAs after annealing displayed a sharp diffraction peak at 25.5° corresponding to the (101) plane of TiO_2 anatase (DB card number 9015929), more significant peaks were observed at the 2θ: 25.5°, 38.6°, 48.2°, 54.3°, 55.3° indexed to (101), (004), (200), (105), (211) planes of tetragonal anatase phases of TiO_2, respectively [58–60] while no peaks were detected for the TiO_2 rutile phase. It is evident from Figure 5, the peak at 23.5° and 42.8° correspond to the plane (002) and (111) of RGO [23]. The XRD patterns of Au-TNTs and RGO/Au-TNTAs samples displayed two noteworthy major diffraction peaks at 2θ: 39.2° and 77.3°, attributed to the (111) and (311) crystal planes of Au, indicating the successful deposition of Au nanoparticles [61,62]. These results were consistent with the standard card values (DB: 9013043). Moreover, from XPS analysis the Ti^{4+} state confirmed the Au metallic nature in the Au-TNTs and RGO/Au-TNTAs nanocomposites [61]. There is no typical diffraction peak of RGO in the RGO/Au-TNTAs sample except plane of (111) at 42.8°, this is mainly attributed to that

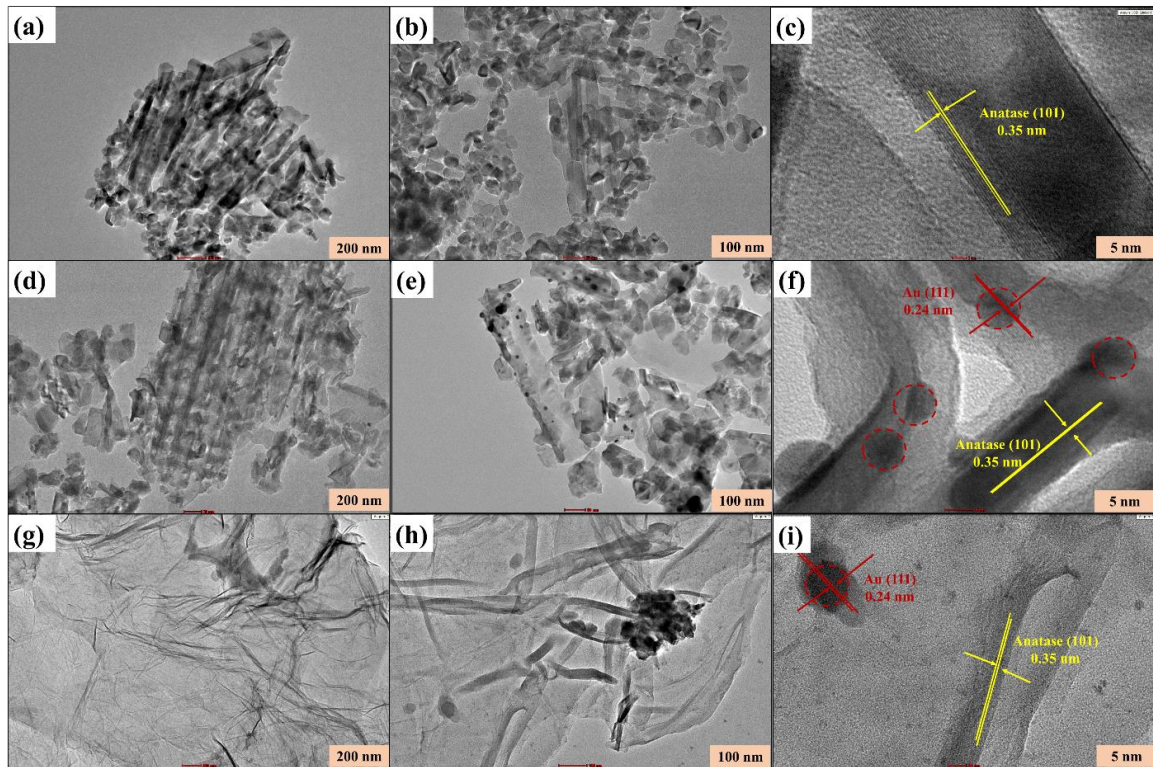the RGO characteristic peak at 25.0° was overlapped with the (101) peak of TiO$_2$ anatase phase [38,63].

Figure 4. HR-TEM images of (**a**,**b**) TNTAs at different magnifications, (**c**) lattice spacing of TNTAs, (**d**,**e**) Au-TNTAs at different magnifications, (**f**) lattice spacing of Au-TNTAs, (**g**,**h**) RGO/Au-TNTAs at different magnification and (**i**) lattice spacing of RGO/Au-TNTAs.
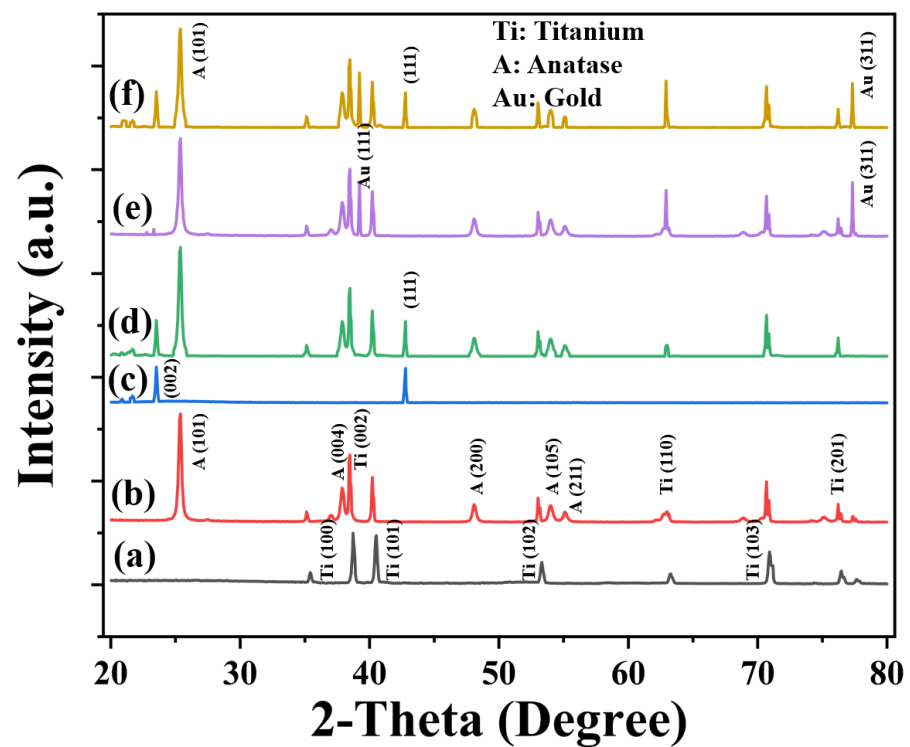

Figure 5. XRD patterns of the (a) Unannealed-TNTAs, (b) Annealed-TNTs, (c) Bare RGO, (d) RGO-TNTs, (e) Au-TNTAs and (f) RGO/Au-TNTAs.

The crystallite size and the *d*-spacing of the synthesized samples were computed using Scherrer and Bragg's equations. Additionally, to determine the crystallite size of TNTAs sharp diffraction peak of 25.5° for (101) crystal plane of anatase TiO_2 was used. The crystallite size for anatase TiO_2 was measured as 31.30 nm which is consistent with the previously reported study by Sim et al. [64]. After the inclusion of Au nanoparticles into the TNTAs matrix, no significant changes in the crystallite size of anatase TiO_2 in pure TNTAs (31.30 nm) and RGO/Au-TNTAs (27.03 nm) were noticed. The crystalline size for Au was determined for the sharp diffraction peak at 39.0° that has a crystal plane (111). The mean crystallite size of Au was determined as ~8 nm.

3.2. Surface Analysis

It is well known that when a material is exposed to infrared radiation, every molecule or chemical structure displays a distinct spectral fingerprint. Therefore, FTIR spectroscopy was employed to identify the functional groups of the prepared samples and the results are presented in Figure 6. The FTIR spectra revealed the successful reduction of the oxygen-containing groups in GO to form RGO as shown in Figure 6 (a,b). The GO exhibited various stretching vibration bands of 3400 cm^{-1} representing the hydroxyl (O-H) group, 1633 cm^{-1} for the unoxidized graphitic domains (C=C), 1384 cm^{-1} for the carboxyl (C-O) group and at 1121 cm^{-1} for alkoxy and epoxy pairs (C-O) [32,56,65]. After the reduction, all the peaks corresponding to the stretching vibration of oxygen-containing functional groups (O-H and C-O) were significantly reduced as a result of the de-oxygenation process [25]. This de-oxygenation has no negative effect on CO_2 photoreduction [23,48]. The RGO peaks in the ternary composite also confirm the good decoration of RGO nanosheets on TNTAs. However, the strong peak appearing at 807 cm^{-1} in pure TNTAs is ascribed to the symmetrical stretching vibration band of TiO_2 (Ti-O-Ti) [32]. The peak between 2500–2250 cm^{-1} for TNTs and Au-TNTs could be due to other oxygen-containing functional groups. The TiO_2 lattice vibration in doped TNTAs moved towards a lower frequency after the addition of Au NPs and RGO nanosheets, indicating the successful development of the ternary RGO/Au-TNTAs nanocomposite. Moreover, the absorption peak at 800 cm^{-1} in RGO/Au-TNTAs is attributed to the Ti-O-C band as a result of the interaction between the functionalities of Au and RGO with TNTAs [32,56,66].

To obtain more detailed information regarding the elemental state and chemical composition of the RGO/Au-TNTAs composite, XPS analysis was performed and depicted in Figure 7. As shown in Figure 7a, the XPS spectra over the prepared TNTAs, Au–TNATs, and RGO/Au–TNTAs samples confirmed the presence of compositional elements (Ti, C, O, Au). The XPS analysis of individual TNTAs, Au–TNTAs and RGO–TNTAs has been provided in supplementary information (see Figures S2–S4). The binding energies of Ti 2p (Figure 7b) in RGO/Au–TNTAs were detected at two identical peaks of 459.07 eV (Ti $2p_{3/2}$) and 464.49 eV (Ti $2p_{1/2}$) which are consistent with the previously reported studies [25,66]. It is worth mentioning that the separation of two peaks of Ti 2p spectra was found at 5.42 eV which confirmed the Ti^{4+} state of anatase TiO_2 [25,47,66]. The O 1s XPS spectrum can be fitted by two chemical states at 530.43 eV and 532.21 eV (Figure 7c). The binding energy peak at 530.43 eV can be ascribed to the Ti-O bond (O lattice), whereas the peak at 532.21 eV corresponds to the oxygen vacancies [25,49]. The C 1s XPS spectra of RGO/Au-TNTAs are presented in Figure 7d and its de-convolution results in four identical peaks located at 284.23, 285.65, 287.88, and 290.96 eV which are attributed to the sp2 hybridized carbon (C=C), epoxy and hydroxyl (C-O), carbonyl (C=O) and carboxylic (O-C=O) groups, respectively. These functional groups suggest that C-O-Ti bonds may be formed when the O-H groups on the TiO_2 surface contact with the carboxyl (COOH) group on RGO [25,67]. The binding energies of Au 4f at 82.84 eV and 89.23 eV are associated with the standard Au $4f_{7/2}$ and Au $4f_{5/2}$ peaks, as portrayed in Figure 7e. The fact that they can be effectively attributed to the Au^0 loaded on TiO_2 and Au NPs are synthesized on the surface of TNTAs in a state of metal [62,68]. Therefore, the XPS analysis revealed that the oxygen vacancy, Ti^{4+} state, and Au^0 donor state are stable in the anatase lattice and functioning as the

prevailing defect. Consequently, this defect state and the LSPR effect of Au NPs in the ternary composite may narrow the bandgap and shift the optical absorption to the visible light range [56,66].
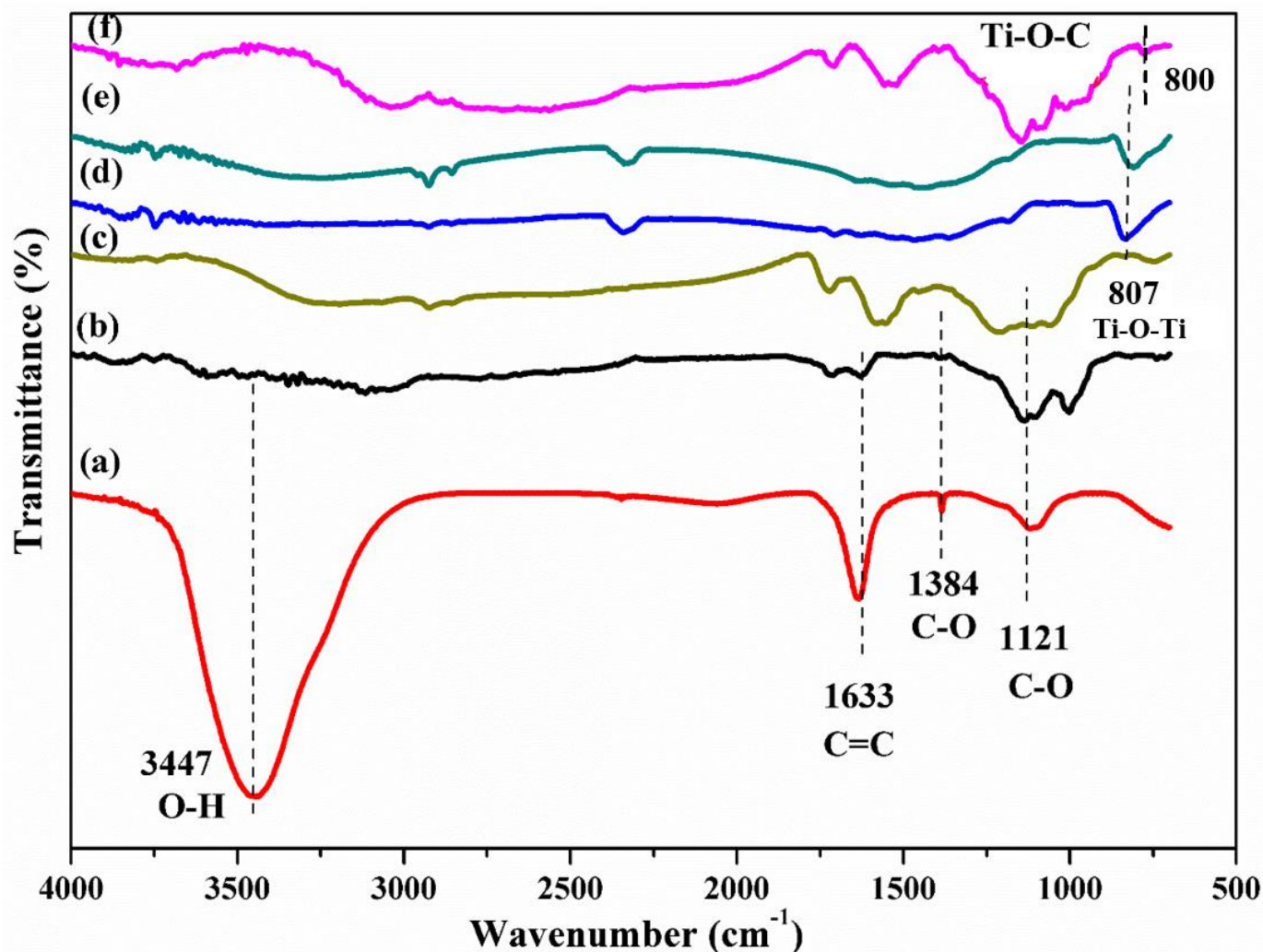

Figure 6. FTIR spectra of (a) GO, (b) RGO, (c) RGO-TNTAs, (d) TNTAs, (e) Au-TNTAs and (f) RGO/Au-TNTAs.

3.3. Optical Analysis

Photoluminescence (PL) analysis was employed for investigating the transfer and separation efficiency of photogenerated charge carriers in the prepared samples. Higher PL emissions are an indication of a higher recombination rate of electron-hole pairs while a lower PL intensity peak refers to suppressed recombination [23,62]. Obviously, the pure TNTAs sample exhibited the highest PL emissions with a sharp peak between 500 and 600 nm as depicted in Figure 8a. However, the PL emissions of TNTAs were greatly decreased by the incorporation of Au NPs. The Au NPs have the LSPR characteristic which can enhance the absorption of light by generating more electron hole pairs (e^-/h^+). The formation of the Schottky junction due to due to the plasmic effect of Au doping also facilitates the charge transfer [69]. The PL emissions were further reduced to a minimum in the presence of RGO nanosheets with the Au-TNTAs composite, revealing the great role of RGO as a solid electron mediator.
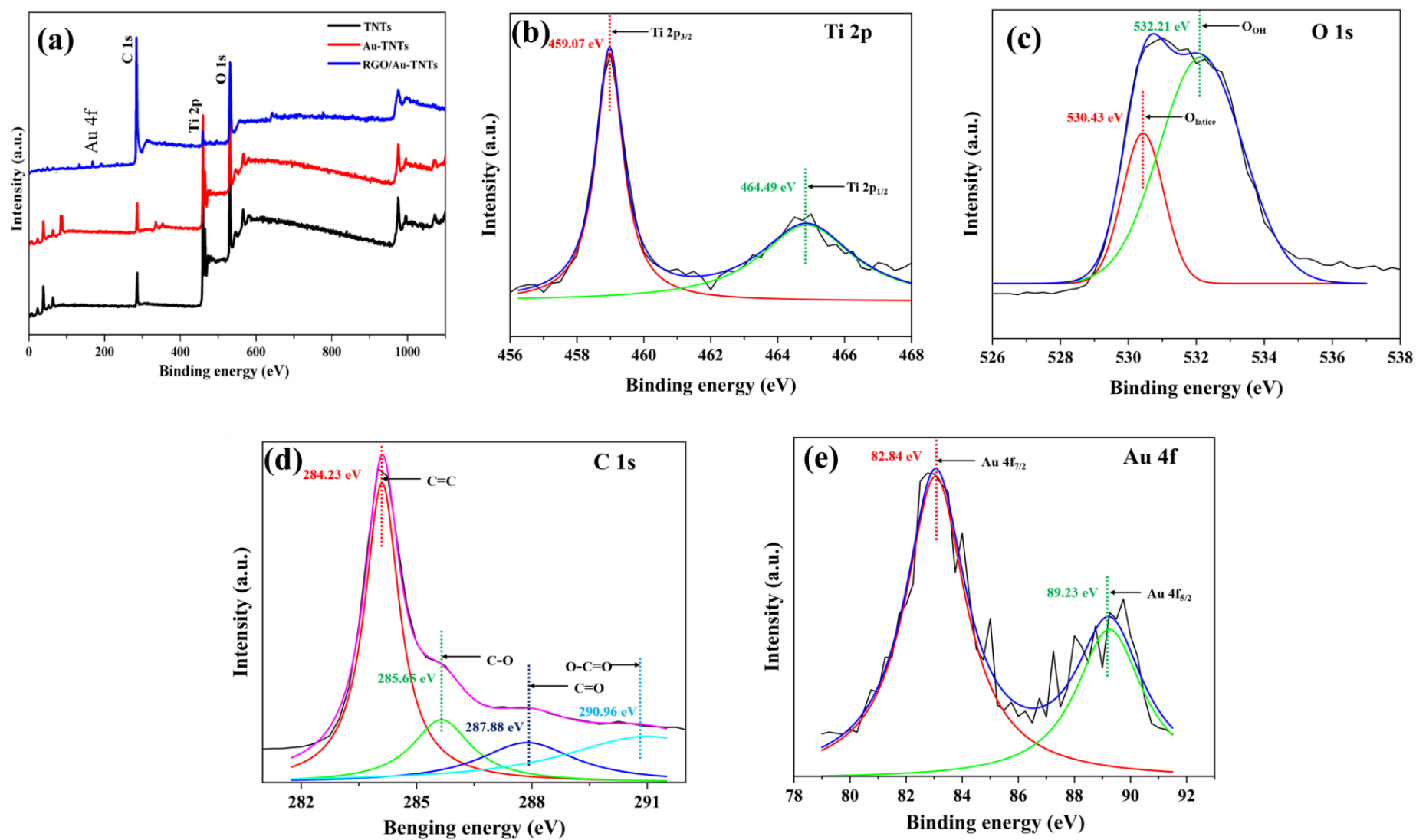
Figure 7. Fully scanned XPS spectra of (**a**) TNTAs, Au-TNTAs, and RGO/Au-TNTAs, Core level XPS spectra of RGO/Au-TNTAs (**b**) Ti 2p, (**c**) O 1s, (**d**) C 1s and (**e**) Au 4f.
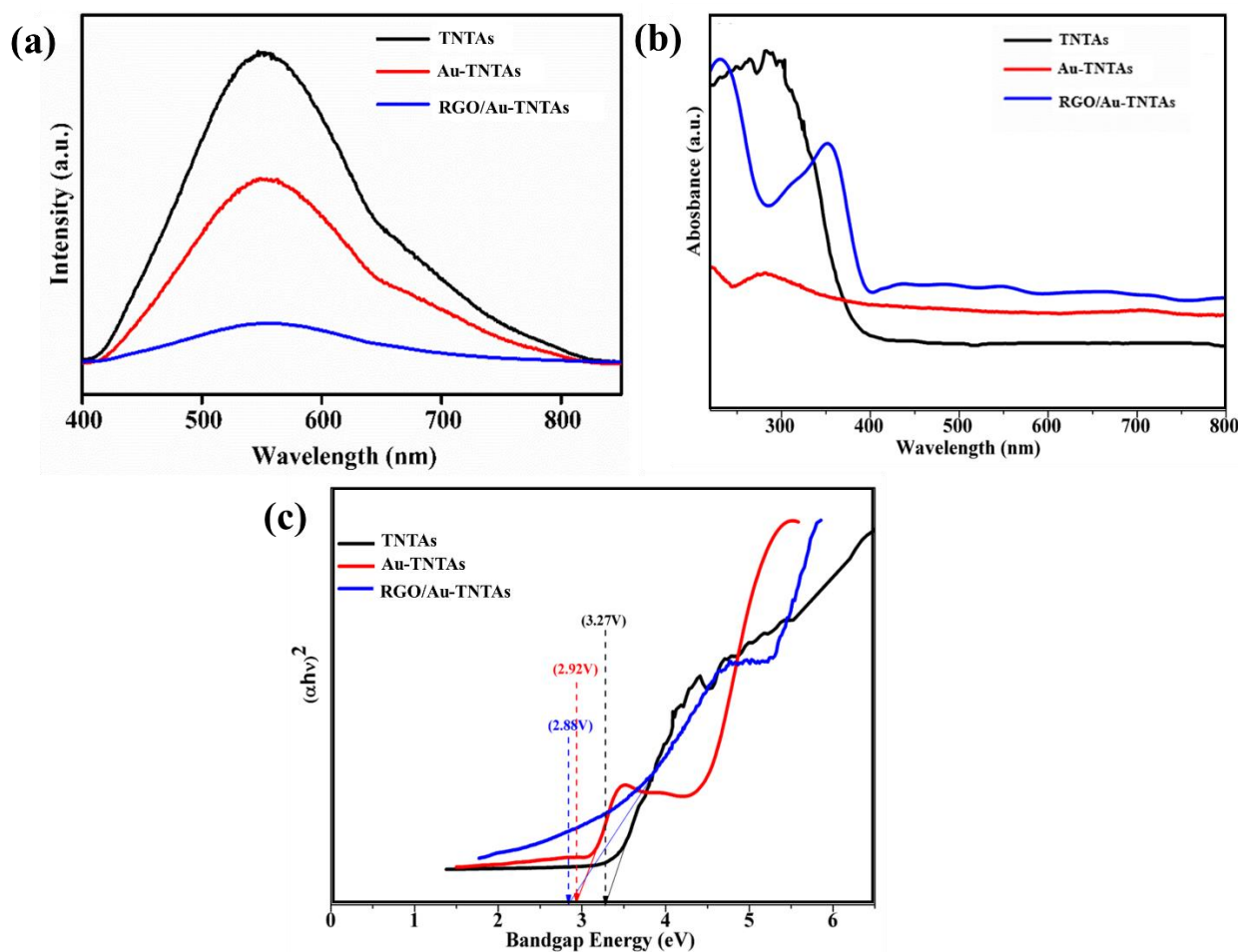
Figure 8. (**a**) PL spectra of pure TNTAs, Au-TNTAs, and RGO/Au-TNTAs, (**b**) UV–vis absorption spectra of pure TNTAs, Au-TNTAs, and RGO/Au-TNTAs and (**c**) Tauc plots of pure TNTAs, Au-TNTAs and RGO/Au-TNTAs.

The UV–vis diffuse reflectance spectroscopy (UV-Vis DRS) is used to determine the light-responsive character of the prepared samples. Figure 8b shows the UV-visible spectra of pure TNTAs, Au-TNTAs, and RGO/Au-TNTAs composite. The un-doped TNTAs displayed an absorption edge at around 380 nm in the UV range as a result of the intrinsic band gap absorption of TiO_2 due to the electron transfer from the VB to the CB (O2p→Ti3d) [70]. Compared to pure TNTAs, the Au-TNTAs and RGO/Au-TNTAs samples exhibited an enhanced light absorption in the range of 400 to 800 nm. Moreover, when Au NPs and RGO nanosheets were deposited on TNTAs, the reduction of band edge to the visible light region was enlarged which is mainly attributed to the LSPR effect [56,71].

To quantify the bandgap of all synthesized photocatalysts, the Tauc plots were obtained in this study, as presented in Figure 8c. Tauc plots were estimated using the Kubelka-Munk transformation function [71]. The detailed process for calculating the band gap of catalytic materials has been provided in supplementary information. The band gap energies of TNTAs, Au-TNTAs, and RGO/Au-TNTAs were found to be 3.27 eV, 2.92 eV, and 2.88 eV, respectively. Clearly, the band gaps of Au-TNTAs and RGO/Au-TNTAs were reduced compared to pure TNTAs. This reduction can be ascribed to the development of a sub-band between the conduction and valance bands of TiO_2 as a result of the addition of Au and RGO, which allowed the electrons to be excited from the VB to the sub-band state by absorbing visible light [32]. The RGO/Au-TNTAs composite has shown a greatly improved ability to absorb visible light, making it a viable photocatalyst for photocatalytic CO_2 reduction.

3.4. Phocatalytic CO2 Reduction Performance

The photocatalytic performance of pure TNTAs and modified TNTAs (Au-TNTAs, RGO-TNTAs, and RGO-Au-TNTAs) photocatalysts were assessed for the photocatalytic CO_2 reduction with H_2O vapor into CH_4 under visible light irradiation. This study only focused on CH_4 production, though other value-added chemicals were also generated during the CO_2 reduction process which is one of the shortcomings of the present study. The photo-reduction experiments were conducted in a fixed-bed gas-phase photoreactor. For quality assurance reasons, a series of control tests were run under different conditions (in the absence of photocatalyst, by using N_2 gas as feed, and by performing reactions in the dark) prior to any experiments to ensure that the products were not generated from the photocatalysts themselves or any other additional side reactions. However, no hydrocarbon products were detected during all control experiments. The rate of CO_2 photoreduction to CH_4 was monitored by collecting samples from the reactor at 1 h intervals and analyzing them using GC-FID. Figure 9a and Table S1, present the photocatalytic production rates of CH_4 over different photocatalysts at different irradiation times. After 4 h of light irradiation, the pure TNTAs photocatalyst exhibited the lowest CH_4 production rate of 1.24 ppm cm^{-2} h^{-1}. This could be explained on the base that the TiO_2 material is known to be insensitive to visible light due to its comparatively wide range of band gaps. However, after doping the TNTAs with RGO, the transfer of electrons was promoted, thus enhancing the CH_4 yield up to 4.41 ppm cm^{-2} h^{-1}. The incorporation with RGO has also reduced the charge recombination rate of TNTAs as it has 2D and planar π-conjugation nanostructure, making it an effective electron-conductive material [72–74]. Moreover, the RGO nanosheets provide a quick pathway for trapping the photoinduced electrons and suppressing the charge carriers' recombination. The Au-TNTAs displayed a notable improvement with a CH_4 production of 8.15 ppm cm^{-2} h^{-1}. The loading of Au NPs into TNTAs has contributed much to generating a higher rate of electrons for enhancing the CO_2 photoreduction activity, owing to the LSPR characteristic of Au NPs [75,76]. Compared to all tested photocatalysts, the ternary RGO/Au-TNTAs nanocomposite exhibited the highest CH_4 production evidenced by GC spectra (Figure S5). The rate is 10.62 ppm cm^{-2} h^{-1}. This photocatalytic enhancement was a result of the combination of the LSPR effect of Au NPs and the RGO electron mediator. The significant improvement obtained by utilizing the RGO/Au-TNTAs as a photocatalyst represented almost 9 times higher amount of produced CH_4 compared to pure TNTAs.

Figure 9b shows the total yield of CH_4 evaluation for 4 h exposure to light irradiation. The total yield of CH_4 follows an ascending order of TNTAs (4.02 ppm cm^{-2}) < RGO-TNTAs (12.46 ppm cm^{-2}) < Au–TNTAs (21.64 ppm cm^{-2}) < RGO/Au–TNTAs (35.13 ppm cm^{-2}). The order of CO_2 photoreduction to CH_4 followed by the photocatalysts was consistent with a previous study conducted by Sim et al. [56].

3.5. Comparison of CO2 Reduction Rate of TNTAs-Based Photocatalysts

The photocatalytic performances of the previously reported TNTAs-based photocatalysts along with the present study have been listed in Table 1. All the important information including the synthesis methods of TNTAs and their composite, photocatalytic reaction conditions, reactants, total yield of products, average rate of production, and enhancement of production rate of composite photocatalysts compared to pure TNTAs are summarized in order to get a clear understanding of the literature with the present work for the comparison of the present results with the previously published studies which considered similar reaction conditions and reactants. The table shows that TNTAs have been employed mostly with noble metals and carbon-based materials to improve CO_2 photoreduction performance. For instance, Ikreedeegh and Tahir [23], Razzaq et al. [46], and Zubair et al. [47] employed carbon-based materials for enhancing the CO_2 reduction rate. The maximum production of CH_4 (3322 µmol m^{-2}), which is 1.94 times higher than pristine TNTs, was attained after 4 h of irradiation utilizing the g-C_3N_4-RGO-TNTAs composite [23]. The photocatalytic CO_2 reduction performance was enhanced 5.6 and 4.4 times compared to

pure TNTAs when modified the photocatalysts using GQDs and RGO, respectively [46,47]. Similar to the present study, Sim et al. [56] and Durga Devi et al. [43] have utilized both noble metals and carbon-based materials to modify TNTAs photocatalysts. Both studies employed Pt as a noble metal, while Sim et al. [56] and Durga Devi et al. [43] utilized RGO and GO as a carbon sources, respectively. However, with the exception of the present study, no other reports are available on the use of TNTAs coupled with Au and RGO for photocatalytic CO_2 reduction under visible light irradiation. Consistent with the present study, both Sim et al. [56] and Durga Devi et al. [43] reported enhanced CO_2 reduction rates as following the order TNTAs > carbon-based material-TNTAs > noble metals-TNTAs.
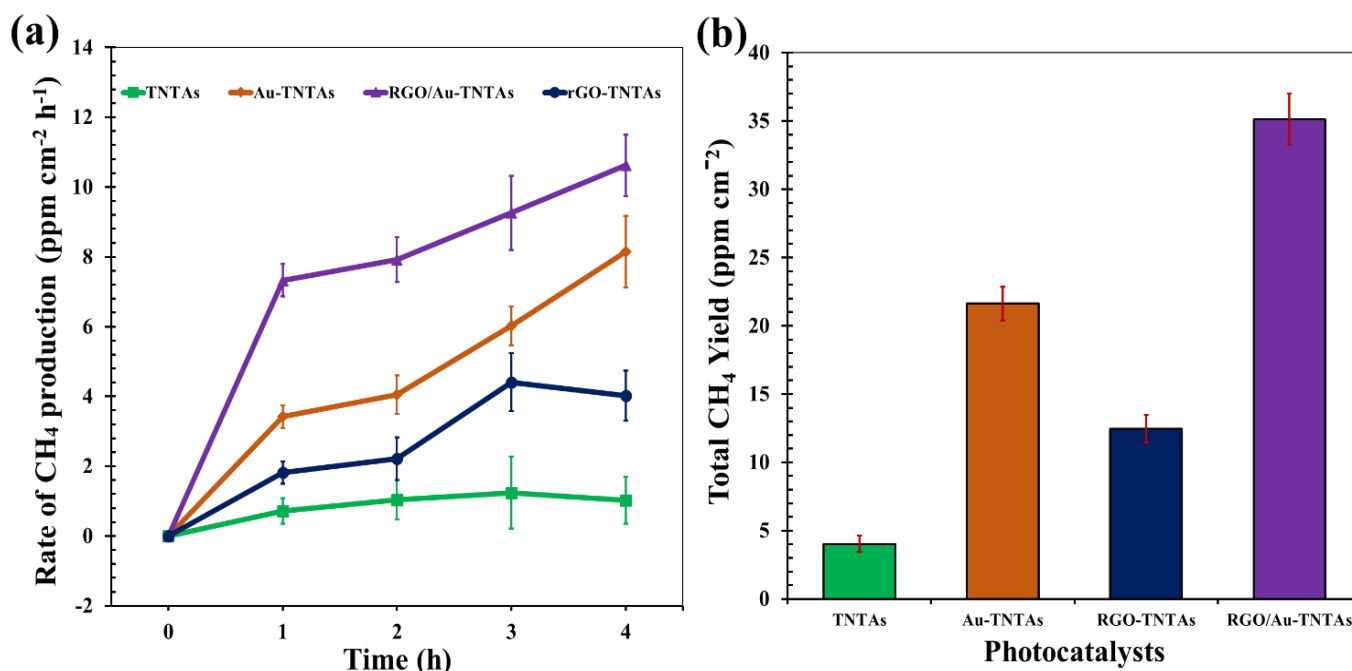

Figure 9. (**a**) Rate of photocatalytic CO_2 reduction with H_2O over TNTAs, Au-TNTAs, RGO-TNTAs, and RGO/Au-TNTAs composite during 4 h irradiation under visible light, (**b**) Total yield of CH_4 over TNTAs, Au-TNTAs, RGO-TNTAs and RGO/Au-TNTAs composite for 4 h irradiation.

In this study, the novel synthesized RGO/Au-TNTAs exhibited elevated photocatalytic CO_2 conversion performance compared to synthesized photocatalysts TNTAs, RGO-TNTAs, and Au-TNTAs. It is evident from Table 1, that the highest enhancement of CH_4 yield (8.75-fold) compared to pure TNTAs was attained in the present study by utilizing the RGO/Au-TNTAs as a photocatalyst. The significantly enhanced photocatalytic performance of CH_4 production is attributed to the successful development of a multi-heterojunction system photocatalyst.
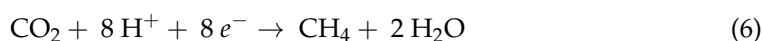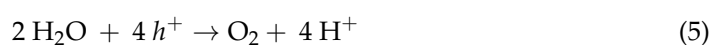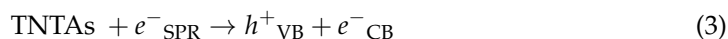
3.6. Proposed Mechanism for Photocatalytic Conversion of CO_2 to CH_4

The photocatalytic performance of any photocatalyst material is solely reliant on its response to light and on the efficiency of charge separation and transfer. However, the product selectivity is dependent on the positions of both the conduction band (CB) and valance band (VB) as well as the number of electrons that participated during the CO_2 photoreduction process [11,77]. For a better understanding of the production of CH_4 through the photocatalytic CO_2 reduction process over the ternary RGO/Au-TNTAs photocatalyst in the presence of water vapor and under visible light, a simple reaction mechanism has been proposed.

Table 1. Comparison of photocatalytic CO_2 reduction to CH_4 by using various TNTAs-based composites.

Photocatalysts	Synthesis Methods of TNTAs and Composite	Photocatalytic Reaction Conditions	Reactants	Total CH_4 Yield	Average Yield Rate	Enhancement of CH_4 Yield Compared to Pure TNTAs	Ref.
TNTAs RGO-TNTs Pt-TNTAs RGO/Pt-TNTAs	Anodization, photo-deposition + immersion	500 W tungsten–halogen lamp visible light 100 W/m^2 5 h	CO_2 + H_2O vapour	5.67 µmol m^{-2} 6.89 µmol m^{-2} 9.03 µmol m^{-2} 10.96 µmol m^{-2}	1.13 µmol m^{-2} h^{-1} 1.38 µmol m^{-2} h^{-1} 1.81 µmol m^{-2} h^{-1} 2.19 µmol m^{-2} h^{-1}	- 1.22-times 1.6-times 1.94-times	[56]
TNTAs RGO-TNTAs	Anodization + electrochemical deposition	100 W Xe lamp visible light 1 h	CO_2 + H_2O vapour	1.28 ppm cm^{-2} 5.67 ppm cm^{-2}	1.28 ppm cm^{-2} h^{-1} 5.67 ppm cm^{-2} h^{-1}	- 4.4-times	[46]
TNTAs GQDs-TNTAs	Anodization + electrochemical deposition	100 W Xe lamp visible light 3 h	CO_2 + H_2O vapour	1.05 ppm cm^{-2} 5.94 ppm cm^{-2}	0.35 ppm cm^{-2} h^{-1} 1.98 ppm cm^{-2} h^{-1}	- 5.6-times	[47]
TNTAs g-C_3N_4-TNTAs g-C_3N_4-GO-TNTAs g-C_3N_4-RGO-TNTAs	Anodization + immersion	35 W Xe lamp visible light 20 mW cm^{-2} 4 h	CO_2+ H_2O vapor	1713.6 µmol m^{-2} 1841.5 µmol m^{-2} 2470.9 µmol m^{-2} 3322.1 µmol m^{-2}	428.4 µmol m^{-2} h^{-1} 460.4 µmol m^{-2} h^{-1} 617.7 µmol m^{-2} h^{-1} 830.5 µmol m^{-2} h^{-1}	- 1.13-times 1.52-times 1.94-times	[23]
TNTAs GO-TNTAs Pt-TNTAs GO/Pt-TNTAs	Anodization + electrophoretic deposition	400 W metal-halide lamp visible light 10 h	CO_2 + H_2O vapour	4700 µmol g^{-1} 11,500 µmol g^{-1} 34,320 µmol g^{-1} 31,430 µmol g^{-1}	470 µmol g^{-1} h^{-1} 1150 µmolg^{-1} h^{-1} 3432 µmol g^{-1} h^{-1} 3143 µmol g^{-1} h^{-1}	- 2.45-times 7.3-times 6.69-times	[43]
TNTAs RGO-TNTAs Au-TNTAs RGO/Au-TNTAs	Anodization, electrochemical-deposition + immersion	300 W Xe lamp visible light 100 W/m^2 4 h	CO_2 + H_2O vapour	4.02 ppm cm^{-2} 12.46 ppm cm^{-2} 21.64 ppm cm^{-2} 35.13 ppm cm^{-2}	1.01 ppm cm^{-2} h^{-1} 3.12 ppm cm^{-2} h^{-1} 5.41 ppm cm^{-2} h^{-1} 8.78 ppm cm^{-2} h^{-1}	- 3.1-times 5.38-times 8.75-times	This study

The bare-TNTAs photocatalyst exhibited poor photocatalytic performance in converting CO_2 to CH_4 due to its low rate of charge transfer under visible light. However, the employing of Au-TNTs as a photocatalyst improved the performance by leveraging the LSPR behaviors of Au, which acted as a virus-like particles (VLPs) sensitizer with the TNTAs [35]. The surface plasmonic oscillation of Au took place with the incident photon energy generated by the light source which delocalized the Au NPs electrons and created multiple SPR-enhanced heterojunctions which improved the efficiency of electron-hole separation [56,78].

$$e^-_{Au} + hv(\text{visible}) \rightarrow e^-_{SPR} \tag{2}$$

$$\text{TNTAs} + e^-_{SPR} \rightarrow h^+_{VB} + e^-_{CB} \tag{3}$$

$$e^-_{CB} + \text{RGO} \rightarrow e^-_{RGO} \tag{4}$$

$$2\,H_2O + 4\,h^+ \rightarrow O_2 + 4\,H^+ \tag{5}$$

$$CO_2 + 8\,H^+ + 8\,e^- \rightarrow CH_4 + 2\,H_2O \tag{6}$$

As illustrated in Figure 10, when the ternary RGO/Au-TNTAs photocatalyst is irradiated with visible light, the light photons are absorbed by the Au NPs as a result of the LSPR effect as shown in Equation (2). The photo-induced electrons in Au are injected into the CB of TNTAs as demonstrated in Equation (3). The electrons (e^-) are then transported from the TNTAs CB to the RGO (Equation (4)), the RGO is serving as an electron reservoir by receiving the electrons from TNTAs CB, in addition to its ability in improving the absorption of visible light, owing to its dark color. The electrons cloud on the RGO reacts with the CO_2 molecules while the holes (h^+) at the TNTAs VB oxidize water to produce hydrogen free radicals (H^+) which then react with the CO_2 to form CH_4 after a series of redox reactions as shown in Equations (5) and (6). The synergetic effect of Au NPs and RGO nanosheets prolonged the lifetime of electrons, enhanced visible light absorption, and increased the surface area for higher CO_2 adsorption on the photocatalysts surface and thus improving the photocatalytic performance over the RGO-Au-TNTAs composite [79,80].
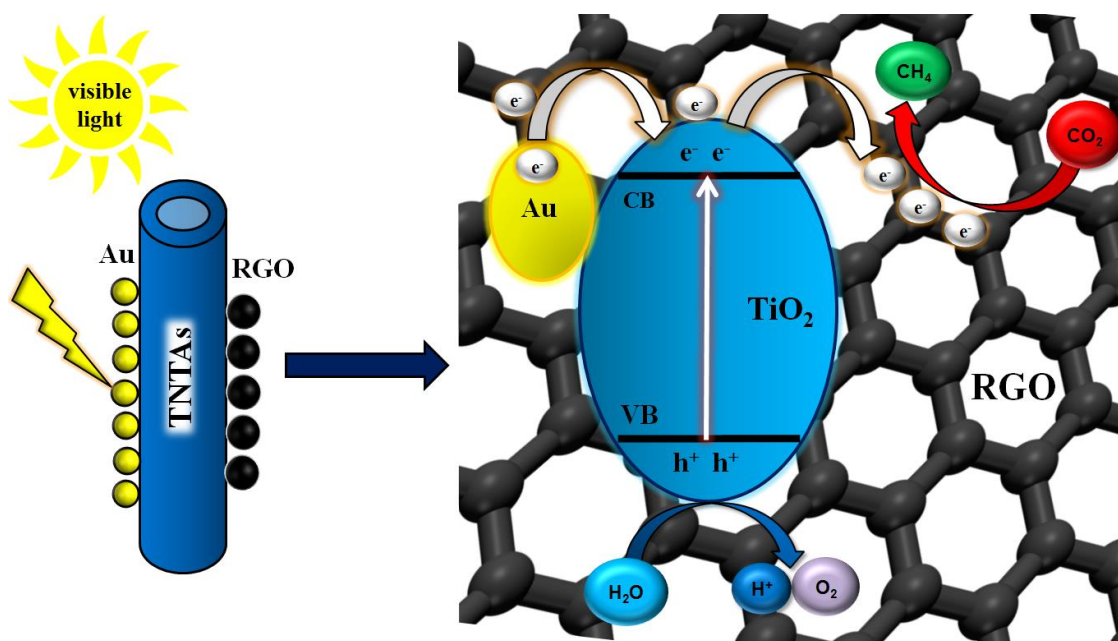

Figure 10. Proposed mechanism for photocatalytic CO_2 reduction to CH_4 over the RGO-Au-TNTAs photocatalysts.

4. Conclusions

In this study, visible light-responsive novel ternary RGO/Au-TNTAs composite photocatalyst was successfully fabricated using a facile approach for CO_2 photoreduction to CH_4. Morphological and elemental investigation revealed that Au NPs and RGO nanosheets were well-deposited into the TNTAs walls. Compared to the pristine TNTAs and binary hybrid composites (Au-TNTAs and RGO-TNTAs), the ternary composite photocatalyst exhibited superior photocatalytic performance. The photocatalytic CO_2 reduction efficiency of RGO/Au-TNTAs to produce CH_4 was about 9 times higher than that of the pure TNTAs. This improvement in photocatalytic performance can be attributed to the LSPR effect of Au NPs and to the facilitation of electron-hole pairs separation by the RGO nanosheets. Similar to the current study, Sim et al. [56] and Durga Devi et al. [43] modified TNTAs photocatalysts using both noble metals and carbon-based materials. Both studies employed Pt as a noble metal, while Sim et al. [56] and Durga Devi et al. [43] utilized RGO and GO as carbon sources, respectively. When compared to those reported studies, the photocatalytic CO_2 conversion performance of the newly synthesized RGO/Au-TNTAs photocatalysts in this study was significantly improved. The present research provides a step forward in the understanding of visible light-generated charge transfer mechanism among the Au NPs, RGO nanosheets, and TNTAs. The constructed novel ternary nanocomposite can be a promising photocatalyst for future applications in the fields of environmental remediation and energy production.

Author Contributions: M.A.H.: Writing—original draft, Methodology, Data curation, Formal analysis, Reviewing and Editing; F.K.: Conceptualization, Methodology, Investigation; R.R.I.: Visualization, Writing—review & editing; A.D.M.: Methodology, Writing; A.A.A.: Funding acquisition, Conceptualization, Supervision; K.H.L.: Writing—review & editing; L.C.S.: Writing—review & editing; W.L.: Conceptualization, Funding acquisition; M.U.M.: Writing—review & editing. All authors have read and agreed to the published version of the manuscript.

Data Availability Statement: Data can be provided by contacting corresponding authors.

Conflicts of Interest: The authors declare no conflict of interest.

References

1. Kumar, K.Y.; Saini, H.; Pandiarajan, D.; Prashanth, M.K.; Parashuram, L.; Raghu, M.S. Controllable synthesis of TiO_2 chemically bonded graphene for photocatalytic hydrogen evolution and dye degradation. *Catal. Today* **2020**, *340*, 170–177. [CrossRef]
2. Liu, Y.; Zhu, Q.; Tayyab, M.; Zhou, L.; Lei, J.; Zhang, J. Single-atom Pt loaded zinc vacancies ZnO–ZnS induced type-V electron transport for efficiency photocatalytic H_2 evolution. *Sol. Rrl* **2021**, *5*, 2100536. [CrossRef]
3. Zhou, Y.; Abazari, R.; Chen, J.; Tahir, M.; Kumar, A.; Ikreedeegh, R.R.; Rani, E.; Singh, H.; Kirillov, A.M. Bimetallic metal–organic frameworks and MOF-derived composites: Recent progress on electro-and photoelectrocatalytic applications. *Coord. Chem. Rev.* **2022**, *451*, 214264. [CrossRef]
4. Wyżga, P.; Tabari, T.; Trochowski, M.; Macyk, W. Optimizing the morphology of titania nanorods for enhanced solar seawater splitting. *Results Eng.* **2023**, *17*, 100921. [CrossRef]

5. Tayyab, M.; Liu, Y.; Min, S.; Irfan, R.M.; Zhu, Q.; Zhou, L.; Lei, J.; Zhang, J. Simultaneous hydrogen production with the selective oxidation of benzyl alcohol to benzaldehyde by a noble-metal-free photocatalyst VC/CdS nanowires. *Chin. J. Catal.* **2022**, *43*, 1165–1175. [CrossRef]

6. Huskinson, B.; Marshak, M.P.; Suh, C.; Er, S.; Gerhardt, M.R.; Galvin, C.J.; Chen, X.; Aspuru-Guzik, A.; Gordon, R.G.; Aziz, M.J. A metal-free organic–inorganic aqueous flow battery. *Nature* **2014**, *505*, 195–198. [CrossRef]

7. Ikreedeegh, R.R.; Tahir, M. A critical review in recent developments of metal-organic-frameworks (MOFs) with band engineering alteration for photocatalytic CO_2 reduction to solar fuels. *J. CO_2 Util.* **2021**, *43*, 101381. [CrossRef]

8. Alkhatib, I.I.; Garlisi, C.; Pagliaro, M.; Al-Ali, K.; Palmisano, G. Metal-organic frameworks for photocatalytic CO_2 reduction under visible radiation: A review of strategies and applications. *Catal. Today* **2020**, *340*, 209–224. [CrossRef]

9. Yoro, K.O.; Daramola, M.O. CO_2 emission sources, greenhouse gases, and the global warming effect. In *Advances in Carbon Capture*; Elsevier: Amsterdam, The Netherlands, 2020; pp. 3–28.

10. Hossen, M.A.; Solayman, H.M.; Leong, K.H.; Sim, L.C.; Nurashikin, Y.; Abd Aziz, A.; Lihua, W.; Monir, M.U. Recent progress in TiO_2-Based photocatalysts for conversion of CO_2 to hydrocarbon fuels: A systematic review. *Results Eng.* **2022**, *16*, 100795. [CrossRef]

11. Ikreedeegh, R.R. Recent developments of Fe-based metal organic frameworks and their composites in photocatalytic applications: Fundamentals; Synthesis and Challenges. *Russ. Chem. Rev.* **2022**, *91*, 1–21.

12. Liu, G.; Feng, M.; Tayyab, M.; Gong, J.; Zhang, M.; Yang, M.; Lin, K. Direct and efficient reduction of perfluorooctanoic acid using bimetallic catalyst supported on carbon. *J. Hazard. Mater.* **2021**, *412*, 125224. [CrossRef]

13. Tahir, B.; Tahir, M.; Amin, N.A.S. Photo-induced CO_2 reduction by CH_4/H_2O to fuels over Cu-modified g-C_3N_4 nanorods under simulated solar energy. *Appl. Surf. Sci.* **2017**, *419*, 875–885. [CrossRef]

14. Fan, W.K.; Tahir, M. Investigating the product distribution behaviour of CO_2 methanation through thermodynamic optimized experimental approach using micro/nano structured titania catalyst. *Energy Convers. Manag.* **2022**, *254*, 115240. [CrossRef]

15. Tu, W.; Zhou, Y.; Zou, Z. Photocatalytic conversion of CO_2 into renewable hydrocarbon fuels: State-of-the-art accomplishment, challenges, and prospects. *Adv. Mater.* **2014**, *26*, 4607–4626. [CrossRef] [PubMed]

16. Tahir, M.; Amin, N.S. Advances in visible light responsive titanium oxide-based photocatalysts for CO_2 conversion to hydrocarbon fuels. *Energy Convers. Manag.* **2013**, *76*, 194–214. [CrossRef]

17. Adekoya, D.; Tahir, M.; Amin, N.A.S. Recent trends in photocatalytic materials for reduction of carbon dioxide to methanol. *Renew. Sustain. Energ. Rev.* **2019**, *116*, 109389. [CrossRef]

18. Anucha, C.B.; Altin, I.; Bacaksiz, E.; Stathopoulos, V.N. Titanium Dioxide (TiO_2)-Based Photocatalyst Materials Activity Enhancement for Contaminants of Emerging Concern (CECs) Degradation: In the Light of Modification Strategies. *Chem. Eng. J. Adv.* **2022**, *10*, 100262. [CrossRef]

19. Tayyab, M.; Liu, Y.; Liu, Z.; Pan, L.; Xu, Z.; Yue, W.; Zhou, L.; Lei, J.; Zhang, J. One-pot in-situ hydrothermal synthesis of ternary $In_2S_3/Nb_2O_5/Nb_2C$ Schottky/S-scheme integrated heterojunction for efficient photocatalytic hydrogen production. *J. Colloid Interface Sci.* **2022**, *628*, 500–512. [CrossRef]

20. Ke, X.; Zhang, J.; Dai, K.; Liang, C. Construction of flourinated-TiO_2 nanosheets with exposed {001} facets/CdSe-DETA nanojunction for enhancing visible-light-driven photocatalytic H_2 evolution. *Ceram. Int.* **2020**, *46*, 866–876. [CrossRef]

21. Cheng, M.; Yang, S.; Chen, R.; Zhu, X.; Liao, Q.; Huang, Y. Copper-decorated TiO_2 nanorod thin films in optofluidic planar reactors for efficient photocatalytic reduction of CO_2. *Int. J. Hydrogen Energy* **2017**, *42*, 9722–9732. [CrossRef]

22. Zhang, Q.; Ye, S.; Song, X.; Luo, S. Photocatalyst based on TiO_2 nanotube arrays co-decorated with CdS quantum dots and reduced graphene oxide irradiated by γ rays for effective degradation of ethylene. *Appl. Surf. Sci.* **2018**, *442*, 245–255. [CrossRef]

23. Ikreedeegh, R.R.; Tahir, M. Photocatalytic CO_2 reduction to CO and CH_4 using g-C_3N_4/RGO on titania nanotube arrays (TNTAs). *J. Mater. Sci.* **2021**, *56*, 18989–19014. [CrossRef]

24. Hossen, M.A.; Solayman, H.M.; Leong, K.H.; Sim, L.C.; Yaacof, N.; Abd Aziz, A.; Lihua, W.; Monir, M.U. A Comprehensive Review on Advances in TiO_2 Nanotube (TNT)-Based Photocatalytic CO_2 Reduction to Value-Added Products. *Energies* **2022**, *15*, 8751. [CrossRef]

25. Rambabu, Y.; Kumar, U.; Singhal, N.; Kaushal, M.; Jaiswal, M.; Jain, S.L.; Roy, S.C. Photocatalytic reduction of carbon dioxide using graphene oxide wrapped TiO_2 nanotubes. *Appl. Surf. Sci.* **2019**, *485*, 48–55. [CrossRef]

26. Santos, J.S.; Fereidooni, M.; Marquez, V.; Arumugam, M.; Tahir, M.; Praserthdam, S.; Praserthdam, P. Single-step fabrication of highly stable amorphous TiO2 nanotubes arrays (am-TNTA) for stimulating gas-phase photoreduction of CO_2 to methane. *Chemosphere* **2022**, *289*, 133170. [CrossRef]

27. Tahir, M. Ni/MMT-promoted TiO_2 nanocatalyst for dynamic photocatalytic H_2 and hydrocarbons production from ethanol-water mixture under UV-light. *Int. J. Hydrogen Energy* **2017**, *42*, 28309–28326. [CrossRef]

28. Azam, M.U.; Tahir, M.; Umer, M.; Jaffar, M.M.; Nawawi, M.G.M. Engineering approach to enhance photocatalytic water splitting for dynamic H_2 production using La_2O_3/TiO_2 nanocatalyst in a monolith photoreactor. *Appl. Surf. Sci.* **2019**, *484*, 1089–1101. [CrossRef]

29. Elysabeth, T.; Agriyfani, D.A.; Ibadurrohman, M.; Nurdin, M. Synthesis of Ni-and N-doped titania nanotube arrays for photocatalytic hydrogen production from glycerol–water solutions. *Catalysts* **2020**, *10*, 1234. [CrossRef]

30. Bu, T.; Liu, X.; Chen, R.; Liu, Z.; Li, K.; Li, W.; Peng, Y.; Ku, Z.; Huang, F.; Cheng, Y.B.; et al. Organic/inorganic self-doping controlled crystallization and electronic properties of mixed perovskite solar cells. *J. Mater. Chem. A* **2018**, *6*, 6319–6326. [CrossRef]

31. Cho, H.; Joo, H.; Kim, H.; Kim, J.E.; Kang, K.S.; Yoon, J. Enhanced photocatalytic activity of TiO_2 nanotubes decorated with erbium and reduced graphene oxide. *Appl. Surf. Sci.* **2021**, *565*, 150459. [CrossRef]

32. Janekbary, K.K.; Gilani, N.; Pirbazari, A.E. One-step fabrication of Ag/RGO doped TiO_2 nanotubes during anodization process with high photocatalytic performance. *J. Porous Mater.* **2020**, *27*, 1809–1822. [CrossRef]

33. Yao, Y.C.; Dai, X.R.; Hu, X.Y.; Huang, S.Z.; Jin, Z. Synthesis of Ag-decorated porous TiO_2 nanowires through a sunlight induced reduction method and its enhanced photocatalytic activity. *Appl. Surf. Sci.* **2016**, *387*, 469–476. [CrossRef]

34. Wang, M.; Pang, X.; Zheng, D.; He, Y.; Sun, L.; Lin, C.; Lin, Z. Nonepitaxial growth of uniform and precisely size-tunable core/shell nanoparticles and their enhanced plasmon-driven photocatalysis. *J. Mater. Chem. A* **2016**, *4*, 7190–7199. [CrossRef]

35. Khatun, F.; Abd Aziz, A.; Sim, L.C.; Monir, M.U. Plasmonic enhanced Au decorated TiO_2 nanotube arrays as a visible light active catalyst towards photocatalytic CO_2 conversion to CH_4. *J. Environ. Chem. Eng.* **2019**, *7*, 103233. [CrossRef]

36. Pan, H.; Wang, X.; Xiong, Z.; Sun, M.; Murugananthan, M.; Zhang, Y. Enhanced Photocatalytic CO_2 Reduction with Defective TiO_2 Nanotubes Modified by Single-Atom Binary Metal Components. *Environ. Res.* **2021**, *198*, 111176. [CrossRef]

37. Montakhab, E.; Rashchi, F.; Sheibani, S. Enhanced photocatalytic activity of TiO_2 nanotubes decorated with Ag nanoparticles by simultaneous electrochemical deposition and reduction processes. *Appl. Surf. Sci.* **2023**, *615*, 156332. [CrossRef]

38. Luo, J.; Li, D.; Yang, Y.; Liu, H.; Chen, J.; Wang, H. Preparation of Au/reduced graphene oxide/hydrogenated TiO_2 nanotube arrays ternary composites for visible-light-driven photoelectrochemical water splitting. *J. Alloys Compd.* **2016**, *661*, 380–388. [CrossRef]

39. Ikreedeegh, R.R.; Tahir, M. Indirect Z-scheme heterojunction of NH_2-MIL-125 (Ti) MOF/g-C_3N_4 nanocomposite with RGO solid electron mediator for efficient photocatalytic CO_2 reduction to CO and CH_4. *J. Environ. Chem. Eng.* **2021**, *9*, 105600. [CrossRef]

40. Ikreedeegh, R.R.; Tahir, M. Facile fabrication of well-designed 2D/2D porous g-C_3N_4–GO nanocomposite for photocatalytic methane reforming (DRM) with CO_2 towards enhanced syngas production under visible light. *Fuel* **2021**, *305*, 121558. [CrossRef]

41. Nasr, M.; Eid, C.; Habchi, R.; Miele, P.; Bechelany, M. Recent progress on titanium dioxide nanomaterials for photocatalytic applications. *ChemSusChem* **2018**, *11*, 3023–3047. [CrossRef]

42. Purabgola, A.; Mayilswamy, N.; Kandasubramanian, B. Graphene-based TiO_2 composites for photocatalysis & environmental remediation: Synthesis and progress. *Environ. Sci. Pollut. Res.* **2022**, *29*, 32305–32325.

43. Devi, A.D.; Pushpavanam, S.; Singh, N.; Verma, J.; Kaur, M.P.; Roy, S.C. Enhanced methane yield by photoreduction of CO_2 at moderate temperature and pressure using Pt coated, graphene oxide wrapped TiO_2 nanotubes. *Results Eng.* **2022**, *14*, 100441. [CrossRef]

44. Khatun, F.; Aziz, A.A.; Kafi, A.K.M.; Sim, L.C. Synthesis and characterization of TiO_2 nanotube using electrochemical anodization method. *Int. J. Eng. Technol. Sci.* **2018**, *5*, 132–139.

45. Marcano, D.C.; Kosynkin, D.V.; Berlin, J.M.; Sinitskii, A.; Sun, Z.; Slesarev, A.; Alemany, L.B.; Lu, W.; Tour, J.M. Improved synthesis of graphene oxide. *ACS Nano* **2010**, *4*, 4806–4814. [CrossRef] [PubMed]

46. Razzaq, A.; Grimes, C.A.; In, S.I. Facile fabrication of a noble metal-free photocatalyst: TiO_2 nanotube arrays covered with reduced graphene oxide. *Carbon* **2016**, *98*, 537–544. [CrossRef]

47. Zubair, M.; Kim, H.; Razzaq, A.; Grimes, C.A.; In, S.I. Solar spectrum photocatalytic conversion of CO_2 to CH_4 utilizing TiO_2 nanotube arrays embedded with graphene quantum dots. *J. CO_2 Util.* **2018**, *26*, 70–79. [CrossRef]

48. Dvorak, F.; Zazpe, R.; Krbal, M.; Sopha, H.; Prikryl, J.; Ng, S.; Hromadko, L.; Bures, F.; Macak, J.M. One-dimensional anodic TiO_2 nanotubes coated by atomic layer deposition: Towards advanced applications. *Appl. Mater. Today* **2019**, *14*, 1–20. [CrossRef]

49. Sim, L.C.; Leong, K.H.; Ibrahim, S.; Saravanan, P. Graphene oxide and Ag engulfed TiO_2 nanotube arrays for enhanced electron mobility and visible-light-driven photocatalytic performance. *J. Mater. Chem. A* **2014**, *2*, 5315–5322. [CrossRef]

50. Low, J.; Qiu, S.; Xu, D.; Jiang, C.; Cheng, B. Direct evidence and enhancement of surface plasmon resonance effect on Ag-loaded TiO_2 nanotube arrays for photocatalytic CO_2 reduction. *Appl. Surf. Sci.* **2018**, *434*, 423–432. [CrossRef]

51. Lee, A.R.; Kim, J.Y. Highly Ordered TiO_2 Nanotube Electrodes for Efficient Quasi-Solid-State Dye-Sensitized Solar Cells. *Energies* **2020**, *13*, 6100. [CrossRef]

52. Li, X.; Yuan, Z.; Wei, X.; Li, H.; Zhao, G.; Miao, J.; Wu, D.; Liu, B.; Cao, S.; An, D.; et al. Application potential of bone marrow mesenchymal stem cell (BMSCs) based tissue-engineering for spinal cord defect repair in rat fetuses with spina bifida aperta. *J. Mater. Sci. Mater. Med.* **2016**, *27*, 77. [CrossRef] [PubMed]

53. Jin, C.; Su, K.; Tan, L.; Liu, X.; Cui, Z.; Yang, X.; Li, Z.; Liang, Y.; Zhu, S.; Yeung, K.W.K.; et al. Near-infrared light photocatalysis and photothermy of carbon quantum dots and au nanoparticles loaded titania nanotube array. *Mater. Des.* **2019**, *177*, 107845. [CrossRef]

54. Shehzad, N.; Tahir, M.; Johari, K.; Murugesan, T.; Hussain, M. A critical review on TiO_2 based photocatalytic CO_2 reduction system: Strategies to improve efficiency. *J. CO_2 Util.* **2018**, *26*, 98–122. [CrossRef]

55. Tayebi, M.; Kolaei, M.; Tayyebi, A.; Masoumi, Z.; Belbasi, Z.; Lee, B.K. Reduced graphene oxide (RGO) on TiO_2 for an improved photoelectrochemical (PEC) and photocatalytic activity. *Sol. Energy* **2019**, *190*, 185–194. [CrossRef]

56. Sim, L.C.; Leong, K.H.; Saravanan, P.; Ibrahim, S. Rapid thermal reduced graphene oxide/Pt–TiO_2 nanotube arrays for enhanced visible-light-driven photocatalytic reduction of CO_2. *Appl. Surf. Sci.* **2015**, *358*, 122–129. [CrossRef]

57. Goddeti, K.C.; Lee, C.; Lee, Y.K.; Park, J.Y. Three-dimensional hot electron photovoltaic device with vertically aligned TiO_2 nanotubes. *Sci. Rep.* **2018**, *8*, 7330. [CrossRef]

58. Zhuang, C.; Song, Z.; Yu, Z.; Zhang, C.; Wang, J.; Liu, Y.; Zhao, Q. Photoelectrochemical performance of TiO_2 nanotube arrays modified with Ni_2P Co-catalyst. *Int. J. Hydrog. Energy* **2021**, *46*, 4981–4991. [CrossRef]
59. Zhang, W.; Liu, Y.; Zhou, D.; Wen, J.; Zheng, L.; Liang, W.; Yang, F. Diffusion kinetics of gold in TiO_2 nanotube arrays for formation of $Au@TiO_2$ nanotube arrays. *RSC Adv.* **2016**, *6*, 48580–48588. [CrossRef]
60. Montakhab, E.; Rashchi, F.; Sheibani, S. Modification and photocatalytic activity of open channel TiO_2 nanotubes array synthesized by anodization process. *Appl. Surf. Sci.* **2020**, *534*, 147581. [CrossRef]
61. Zhang, L.; Qi, H.; Zhao, Y.; Zhong, L.; Zhang, Y.; Wang, Y.; Xue, J.; Li, Y. Au nanoparticle modified three-dimensional network PVA/RGO/TiO2 composite for enhancing visible light photocatalytic performance. *Appl. Surf. Sci.* **2019**, *498*, 143855. [CrossRef]
62. Yang, X.; Chen, Z.; Zhou, D.; Zhao, W.; Qian, X.; Yang, Q.; Sun, T.; Shen, C. Ultra-low Au–Pt Co-decorated TiO_2 nanotube arrays: Construction and its improved visible-light-induced photocatalytic properties. *Sol. Energy Mater. Sol. Cells* **2019**, *201*, 110065. [CrossRef]
63. Jumeri, F.A.; Lim, H.N.; Zainal, Z.; Huang, N.M.; Pandikumar, A. Titanium dioxide-reduced graphene oxide thin film for photoelectrochemical water splitting. *Ceram. Int.* **2014**, *40*, 15159–15165.
64. Sim, L.C.; Koh, K.S.; Leong, K.H.; Chin, Y.H.; Abd Aziz, A.; Saravanan, P. In situ growth of g-C_3N_4 on TiO_2 nanotube arrays: Construction of heterostructures for improved photocatalysis properties. *J. Environ. Chem. Eng.* **2020**, *8*, 103611. [CrossRef]
65. Chen, D.; Feng, H.; Li, J. Graphene oxide: Preparation, functionalization, and electrochemical applications. *Chem. Rev.* **2012**, *112*, 6027–6053. [CrossRef] [PubMed]
66. Niu, X.; Yan, W.; Zhao, H.; Yang, J. Synthesis of Nb doped TiO_2 nanotube/reduced graphene oxide heterostructure photocatalyst with high visible light photocatalytic activity. *Appl. Surf. Sci.* **2018**, *440*, 804–813. [CrossRef]
67. Wang, W.; Yu, J.; Xiang, Q.; Cheng, B. Enhanced photocatalytic activity of hierarchical macro/mesoporous TiO_2–graphene composites for photodegradation of acetone in air. *Appl. Catal. B* **2012**, *119*, 109–116. [CrossRef]
68. Zhang, G.; Miao, H.; Hu, X.; Mu, J.; Liu, X.; Han, T.; Fan, J.; Liu, E.; Yin, Y.; Wan, J. A facile strategy to fabricate Au/TiO_2 nanotubes photoelectrode with excellent photoelectrocatalytic properties. *Appl. Surf. Sci.* **2017**, *391*, 345–352. [CrossRef]
69. Bai, X.; Yang, Y.; Zheng, W.; Huang, Y.; Xu, F.; Bao, Z. Synergistic photothermal antibacterial therapy enabled by multifunctional nanomaterials: Progress and perspectives. *Mater. Chem. Front.* **2023**, *7*, 355–380. [CrossRef]
70. Abdullah, H.; Khan, M.M.R.; Ong, H.R.; Yaakob, Z. Modified TiO_2 photocatalyst for CO_2 photocatalytic reduction: An overview. *J. CO_2 Util.* **2017**, *22*, 15–32. [CrossRef]
71. Du, Y.B.; Wang, N.; Li, X.N.; Li, J.; Wu, L.P.; Peng, Q.M.; Li, X.J. A facile synthesis of C_3N_4-modified TiO_2 nanotube embedded Pt nanoparticles for photocatalytic water splitting. *Res. Chem. Intermed.* **2021**, *47*, 5175–5188. [CrossRef]
72. Kumar, P.; Boukherroub, R.; Shankar, K. Sunlight-driven water-splitting using two-dimensional carbon based semiconductors. *J. Mater. Chem. A* **2018**, *6*, 12876–12931. [CrossRef]
73. Xiang, Q.; Yu, J.; Jaroniec, M. Enhanced photocatalytic H_2 production activity of graphene-modified titania nanosheets. *Nanoscale* **2011**, *3*, 3670–3678. [CrossRef] [PubMed]
74. Li, Y.H.; Tang, Z.R.; Xu, Y.J. Multifunctional graphene-based composite photocatalysts oriented by multifaced roles of graphene in photocatalysis. *Chin. J. Catal.* **2022**, *43*, 708–730. [CrossRef]
75. Zheng, H.; Zhang, S.; Liu, X.; O'Mullane, A.P. The application and improvement of TiO_2 (titanate) based nanomaterials for the photoelectrochemical conversion of CO_2 and N_2 into useful products. *Catal. Sci. Technol.* **2021**, *11*, 768–778. [CrossRef]
76. Ciocarlan, R.G.; Blommaerts, N.; Lenaerts, S.; Cool, P.; Verbruggen, S.W. Recent Trends in Plasmon-Assisted Photocatalytic CO_2 Reduction. *ChemSusChem* **2023**, *16*, e202201647. [CrossRef]
77. Fu, J.; Jiang, K.; Qiu, X.; Yu, J.; Liu, M. Product selectivity of photocatalytic CO_2 reduction reactions. *Mater. Today* **2020**, *32*, 222–243. [CrossRef]
78. Feng, S.; Wang, M.; Zhou, Y.; Li, P.; Tu, W.; Zou, Z. Double-shelled plasmonic Ag-TiO_2 hollow spheres toward visible light-active photocatalytic conversion of CO_2 into solar fuel. *Appl. Mater.* **2015**, *3*, 104416. [CrossRef]
79. Tahir, M.; Tahir, B.; Amin, N.A.S. Gold-nanoparticle-modified TiO_2 nanowires for plasmon-enhanced photocatalytic CO_2 reduction with H_2 under visible light irradiation. *Appl. Surf. Sci.* **2015**, *356*, 1289–1299. [CrossRef]
80. Xu, Q.; Xia, Z.; Zhang, J.; Wei, Z.; Guo, Q.; Jin, H.; Tang, H.; Li, S.; Pan, X.; Su, Z.; et al. Recent advances in solar-driven CO_s reduction over g-C3N4-based photocatalysts. *Carbon Energy* **2023**, *5*, e205. [CrossRef]